Enhancing singlet oxygen photocatalysis with plasmonic nanoparticles

Alexandra Gellé,[§] Gareth D. Price,[§] Frédéric Voisard,[†] Nicolas Brodusch,[†] Raynald Gauvin,[†] Zacharias Amara,[‡]* and Audrey Moores[§†]*

[§] Centre for Green Chemistry and Catalysis, Department of Chemistry, McGill University, 801 Sherbrooke Street West, Montreal, QC, H3A 0B8, Canada.
[†] Department of Mining and Materials Engineering, McGill University, 3610 University Street, Montreal, QC H3A 0C5, Canada
[‡] Équipe de Chimie Moléculaire, Laboratoire de Génomique, Bioinformatique et Chimie Moléculaire, (GBCM), EA7528, Conservatoire National des Arts et Métiers, HESAM Université, 2 rue Conté, 75003 Paris Cedex 03, France.
*Corresponding authors : Zacharias Amara : zacharias.amara@lecnam.net and Audrey Moores : audrey.moores@mcgill.ca

Abstract

Photocatalysts able to trigger the production of singlet oxygen species are the topic of intense research efforts in organic synthesis. Yet challenges still exist in improving their activity and optimizing their use. Herein, we exploited the benefits of plasmonic nanoparticles to boost the activity of such photocatalysts *via* an antenna effect in the visible range. We synthesized silica-coated silver nanoparticles ($Ag@SiO_2$ NPs), with silica shells which thicknesses ranged from 7 to 45 nm. We showed that they served as plasmonically active supports for tris(bipyridine)ruthenium(II), $[Ru(bpy)_3]^{2+}$, and demonstrated an enhanced catalytic activity under white LEDs irradiation for citronellol oxidation, a key step in the commercial production of the fragrance rose oxide. A maximum enhancement of the plasmon-mediated reactivity of approximatively 3-fold was observed with a 28 nm silica layer along with a 4-fold enhancement in the emission intensity of the photocatalyst. Using electron energy loss spectroscopy (EELS) and boundary elements method simulations, we mapped the decay of the plasmonic signal around the Ag core, and provided a rationale for the observed catalytic enhancement. This work provides a systematic analysis of the promising properties of plasmonic NPs used as catalysis-enhancing supports for common homogenous photocatalysts, and a framework for the successful design of such systems in the context of organic transformations.

KEYWORDS: photocatalysis, plasmonic antenna, field enhancement, $Ru(bpy)_3^{2+}$, singlet oxygen, plasmonic catalysis

Introduction

Visible light photocatalysis is currently at the heart of intense research developments,[1] in particular in the fields of energy,[2] pollution remediation[3] and organic transformations.[4] Photocatalysis is often praised as a method enabling high energy-efficiency and chemical selectivity, complying with the principles of green chemistry.[1, 5] Many visible light photocatalysts have been developed, based on nanomaterials,[6] 2D structures,[7] metal organic frameworks,[8] organometallic complexes[9] or organic molecules.[10] Among the most popular molecular photocatalysts used in organic synthesis, tris(bipyridine)ruthenium(II), $[Ru(bpy)_3]^{2+}$, stands out for a number of reasons. It has the ability to catalyse a large variety of organic [11-13] and inorganic[14] reactions, and it absorbs in the visible range. It has shown superior performances compared to other organometallic and organic photocatalysts in a variety of organic transformations.[15,16, 17] $[Ru(bpy)_3]^{2+}$ also features excellent phosphorescence properties, thanks to its ability to facilitate intersystem crossing in the excited state, which is key to enable energy transfer reactions.[18] Finally $[Ru(bpy)_3]^{2+}$ features good resistance to photobleaching and is thus stable under catalytic conditions, especially as compared to organo-photocatalysts.[18, 19]

$[Ru(bpy)_3]^{2+}$ has been particularly efficient towards the generation of singlet oxygen ($^1O_2$), a powerful manifold for oxidative chemistry, even on complex substrates.[20] This reactivity has been particularly useful in organic transformations, especially the Schenck-ene reaction, which allows the selective oxidation of citronellol, a key step in the manufacturing of the commercial fragrance rose oxide performed on a 100 T/year[21] scale, and the production of artemisin, a major antimalarial drug.[22] Yet, as a member of the platinum series, Ru remains expensive and fairly toxic.[23] There is therefore a need to develop new methodologies to enhance the performance of such molecular photocatalysts, so as to limit the quantity used in the process.[19, 24]

Plasmonic nanoparticles (PNPs) strongly interact with light *via* a phenomenon called localized surface plasmon resonance (LSPR), and have found applications[25] in spectroscopy,[26] nanomedicine,[27] optoelectronics, energy conversion[28] and catalysis.[29-34] PNPs are, among other effects, able to act as antennae modulating and concentrating light in their immediate vicinity.[35, 36] This property is at the heart of surface enhanced Raman spectroscopy (SERS) and surface plasmon resonance (SPR) spectroscopy techniques.[37-41] The antenna effect enabled by PNPs has been exploited to tweak the selectivity and activity of metal based catalysts.[42, 43] As early as 1968, Drexhage and coworkers foresaw the potential of associating PNPs to fluorophores, when witnessing the altered optical properties of a Eu complex in the proximity of a plasmonic Ag film.[44] This first observation of metal enhanced luminescence (MEL) led to numerous applications in biology, including extensive studies by the Geddes and Lakowicz groups.[37, 45-47] The Heyne group has recently studied silica covered Au and Ag PNPs decorated with Rose Bengal (RB) towards the generation of $^1O_2$ for antibacterial activity.[48] They have studied in depth the role of the PNP metal by comparing Ag and Au performances,[48,49] as well as the influence of the PNP shape on photocatalysis enhancement.[50] Moreover, they noticed that in all systems, there was an optimal shell thickness at which the LSPR effect was maximal. Interestingly, the thickness at which the maximum RB luminescence was measured slightly differed from the one at which $^1O_2$ production peaked. Mendoza *et al.* have further studied similar silica covered Au PNPs and analyzed $^1O_2$ generation by three independent methods to conclude that the SPR promoted of

the absorption, intersystem crossing and triplet state generation in the RB photosynthesizer.[51] Other groups studied similar systems with $[Ru(bpy)_3]^{2+}$ or fluorescein isothiocyanate.[52-54] Non rigid spacers such as human serum albumin[55], phospholipid membrane[56] and DNA[57] were also used to immobilized dyes at the surface of PNPs. Despite these developments, the application of this strategy for catalysis has been scarce. Mori *et al.* reported in 2010 the use of $Ag@SiO_2$ NPs decorated with $[Ru(bpy)_3]^{2+}$ for the oxidation of styrene.[58] More recently, Reinhard and coworkers used a phospholipid membrane-covered Ag NP to deposit $[Ru(bpy)_3]^{2+}$ and demonstrated its efficiently for light-enhanced urea degradation.[56] Yet, considering the importance of $^1O_2$ methodologies in the pharmaceutical industry, more work is needed into establishing a structure/activity relationship, and studying the mechanism of this enhancement in the specific context of these organic transformations. [20] As highlighted in a recent review by Linic and coworkers, such hybrid plasmonic materials relying on a plasmonic antenna to boost catalysts are a promising venue for the development of new plasmon-mediated catalysts.[59]

We thus synthesized silica coated Ag PNPs decorated with $[Ru(bpy)_3]^{2+}$, and studied their luminescence and catalytic activity towards citronellol oxidation. In particular, we carefully tuned the silica layer thickness as a mean to control the distance between the supporting PNP and the catalytically active species. Here, immobilisation was performed by simple absorption onto the silica surface, following a strategy developed in our group (Amara) [60, 61] and simplifying past approaches relying on covalent bonding.[58] Photocatalysis for this reaction under optimized conditions was enhanced by the presence of plasmonic core, affording an almost 3-fold enhancement in reaction yield. The shell thickness affording the maximum for luminescence emission for $[Ru(bpy)_3]^{2+}$ was found to be 33 nm while the maximum catalytic enhancement was observed at 28 nm. In order to shed light onto the mechanism of plasmonic enhancement, we conducted a thorough LSPR mapping study using scanning transmission electron microscopy - electron energy loss spectroscopy (STEM-EELS).

Results and discussion

Synthesis of plasmon-active supports for photocatalysis

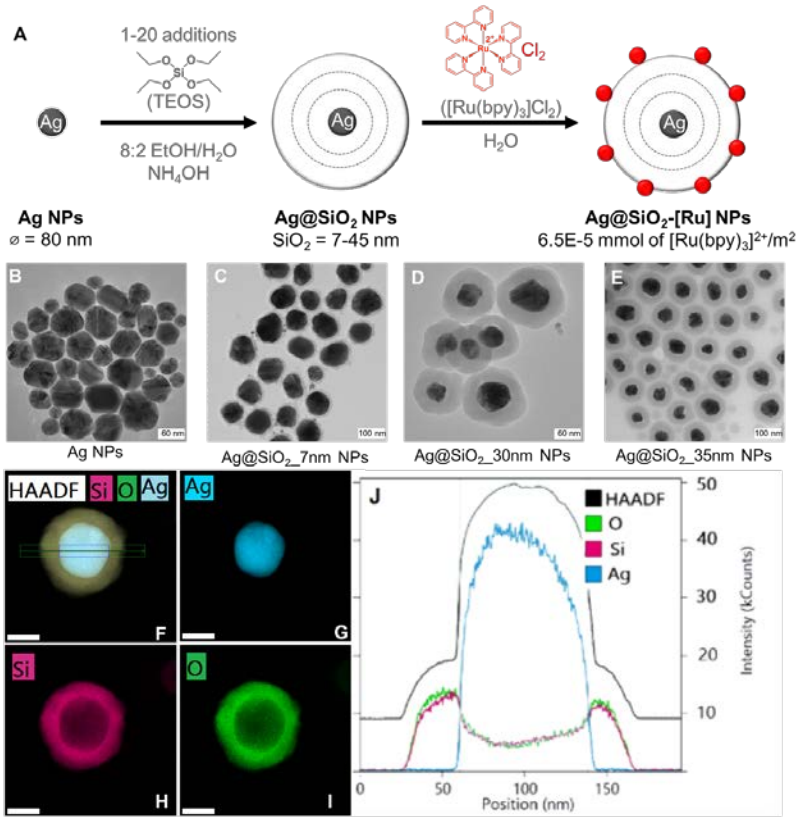

Figure 1A) Synthesis of the silver plasmonic nanoparticles core with a silica shell and immobilization of the photocatalyst $[Ru(bpy)_3]^{2+}$
B-E) TEM images of Ag NPs (1B) and $Ag@SiO_2$ NPs with various thicknesses 1C-E (7 nm, 30 nm and 37 nm) F) High-angle annular dark-field image (HAADF), overlaid with EDS mapping for Ag (blue), Si (pink), and O (green) of an individual $Ag@SiO_2$ NP with a 28 nm shell thickness; G-I) EDS mapping of the same particle for Ag, Si and O; J) Intensity for HAADF and EDS of Ag, O and Si across the linescan shown in G. Scale bars for F), G), H), and I) is 50 nm.

For this study, Ag was selected as the plasmonic metal, since it had been shown to exhibit better field enhancement performances than Au, which was proven to be key for metal-enhanced luminescence.[33, 62, 63] We designed Ag NPs covered with a silica layer, $Ag@SiO_2$ NPs, to serve as supports for photocatalyst $[Ru(bpy)_3]^{2+}$ thus affording $Ag@SiO_2$-[Ru] (Figure 1A). Briefly, Ag NPs were first synthesized using $AgNO_3$ as a precursor and polyvinylpyrrolidone (PVP) as a capping agent following previously reported methods (see SI for details).[64] The Ag NPs were then coated with SiO_2 *via* the Stöber process, which consists of repeated addition and hydrolysis of tetraethyl orthosilicate (TEOS) until reaching the desired silica shell thickness.[65] Following this step, $Ag@SiO_2$ were decorated with $[Ru(bpy)_3]^{2+}$ taking advantage of electrostatic interactions, and provided access to $Ag@SiO_2$-[Ru].[60, 66, 67]
In this design, Ag was selected as the plasmonic metal, since it had been shown to exhibit better luminescence enhancement performances than Au.[62, 63] We initially optimized the Ag core diameter and the thickness of the silica shell to ensure that the SPR signal effectively overlapped with $[Ru(bpy)_3]^{2+}$, which has a maximum absorption at 450 nm.[68] Indeed, recent studies

suggested that MEL was strongly favored by a good overlap between the SPR band and the excitation band of the photocatalyst.[46, 57, 69-72] In particular, we made sure that this overlap remained good across a range of silica shell thicknesses. This initial study allowed to identify an Ag core of 80 nm in diameter, with a shell of 25-35 nm, as a good fit. Afterwards, we optimized the amount of photocatalyst immobilized on the surface to maximise the luminescence of the photosynthesizer (See complete discussion in section 2 ESI).

$Ag@SiO_2$ and $Ag@SiO_2$-[Ru] NPs characterization

Transmission electron microscopy (TEM) analysis of the resulting $Ag@SiO_2$ NPs confirmed the formation of Ag cores with diameters of 80.4 ± 8.1 nm (Figure 1B). Their silica shells featured thicknesses of 7 (Figure 1C), 10, 15, 19, 25, 28, 30 (Figure 1D), 33, 37 (Figure 1E), 40 or 45 nm, a parameter we could control *via* the number of TEOS additions. In all cases, the particles core and shells were very uniform across samples, with no core-free particles or irregular shells observed. High-angle annular dark-field image (HAADF) (Figure 1G) and mapping by Energy Dispersive X-Ray Spectroscopy (EDS) (Figures 1H-J) confirmed the presence of the silver core surrounded by a shell made of Si and O of approximatively 28 nm as measured on the TEM images. We then evaluated the specific surface of $Ag@SiO_2$ NPs by Brunauer−Emmett−Teller (BET) measurements. It ranged from 4 m^2/g to 21 m^2/g for shells of 7 nm to 45 nm, respectively (Table S1 ESI). While the variation in specific surface area was small, it did increase as the particle size grow, which is counter intuitive. We attributed it to surface roughening as layers of silica were added, as we found in an earlier report. The total pore volume obtained from the BJH method is in the order of E-05 cm^3/g, indicating the absence of a porous network in the material. During subsequent $[Ru(bpy)_3]^{2+}$ immobilization, care was taken to control their density per surface unit, as a way to maintain two consecutive photocatalysts at a similar distance, on average. Upon optimization (see ESI section 2), the value of 6.5 10^{-5} mmol of $[Ru(bpy)_3]^{2+}/m^2$ of support was kept constant for all $Ag@SiO_2$ NP samples. Indeed, it is well known that photoactive molecules may undergo self-quenching when they are in close proximity, thus this parameter was considered the most important one to lock for comparison purposes.[73] The subsequent immobilization of $[Ru(bpy)_3]^{2+}$ onto the silica shell was evaluated by ζ -potential measurements (Table S2 ESI). The naked $Ag@SiO_2$ NP surface featured a negatively charged surface of -29.0 mV, a value which dropped to -17.2 mV upon functionalization with $[Ru(bpy)_3]^{2+}$. The amount of photocatalyst immobilized at the surface of $Ag@SiO_2$ NPs was determined by UV-Vis absorption spectroscopy, by subtracting the concentrations of $[Ru(bpy)_3]^{2+}$ before and after exposure to the support. Optimal immobilization was achieved when collected supernatants were colorless.

Optical properties

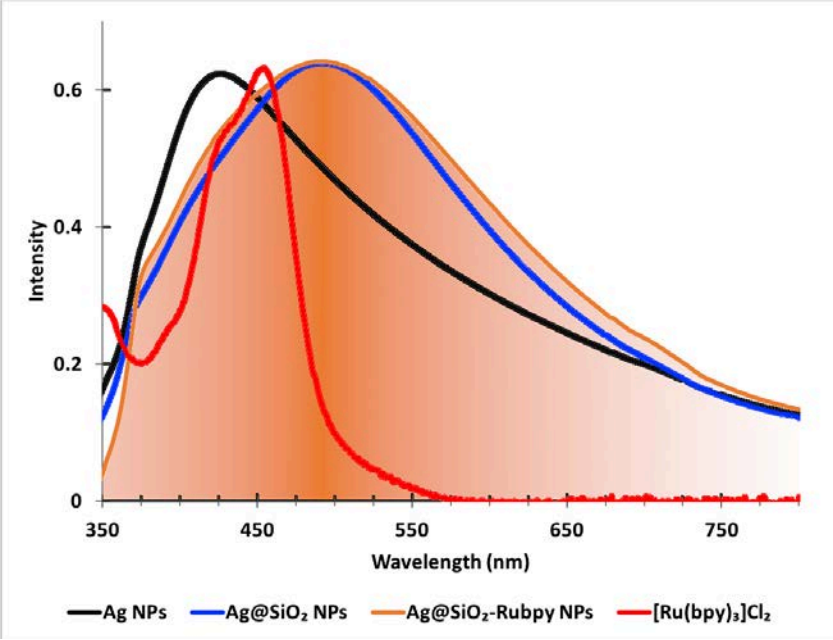

Figure 2 – Normalized extinction spectra of studied photoactive systems in ethanol. Black line: Ag NPs; blue line: $Ag@SiO_2$; red line: homogeneous $[Ru(bpy)_3]Cl_2$; orange gradient $Ag@SiO_2$-[Ru].

Prior to silica coating, the core Ag NPs featured a plasmonic band centered at 420 nm Figure 2-black). Upon silica layer growth, the plasmon band of $Ag@SiO_2$ NPs redshifted (Figure S4) and broadened (Figure 2-blue) as an effect of dielectric medium change at the vicinity of the Ag core.[74-76] As the photocatalyst was immobilized at the surface of $Ag@SiO_2$ NPs, the extinction profile of the ensemble enveloped both the SPR band and the absorption of $[Ru(bpy)_3]^{2+}$ (Figure 2 – red and orange). The immobilization of $[Ru(bpy)_3]^{2+}$ hardly affected the position of the SPR band of the PNPs, yet it caused a small broadening, as reported before.[77-79]
In order to evaluate the ability of the synthesized plasmon-active nanosupports to enhance the optical properties of $[Ru(bpy)_3]^{2+}$, we turned to fluorescence measurements. First, we irradiated $Ag@SiO_2$-[Ru] samples, at the excitation wavelength of $[Ru(bpy)_3]^{2+}$, namely 450 nm, and the intensity of the luminescence was measured at its emission wavelength, 615 nm. The photoluminescence properties were studied for silica layers ranging from 7 to 45 nm with an identical concentration of photocatalysts immobilized on commercial SiO_2 NPs (figure S5). For all samples with medium and large silica shell, we observed an emission peak, which confirms the presence of $[Ru(bpy)_3]^{2+}$ onto the $Ag@SiO_2$ NPs and the preservation of its luminescence (figure S5).

For a given $[Ru(bpy)_3]^{2+}$ surface coverage, its emission intensity was strongly dependant on the thickness of the silica shell. In order to establish a clear comparison framework, we calculated an enhancement factor for each support (Equation S4). It is defined as the ratio between the intensity measured for each system and the one for commercial 80 nm SiO_2 NPs, without metallic core, decorated with the photocatalyst (SiO_2-[Ru]).

The trend in emission intensity observed when varying the shell thickness (figure 3 orange dotted line) is in agreement with previous studies by the Heyne group, on the effect of plasmonic enhancement on the emission of Rose Bengal immobilized on $Ag@SiO_2$ NPs.[48, 50] For very thin SiO_2 layers, the photocatalyst experienced a significant non radiative decay[38] and the emission was strongly quenched, presumably due to charge transfer between the photocatalyst and the metal. As we increased the shell thickness, the emission intensity started to increase significantly, until reaching a maximum for NPs decorated with $[Ru(bpy)_3]Cl_2$ with a layer of a 33 nm. Under these conditions, the catalysts were no longer quenched by the metal surface, thus allowing radiative pathways to take place. The increase in emission intensity was attributed to the enhanced electric field caused by the plasmonic Ag core, which boosts the excitation of the fluorophore and its emission. The maximum luminescence enhancement corresponded to a 4-fold increase, as compared to $[Ru(bpy)_3]^{2+}$ immobilized on commercial SiO_2. For thicker shells, the emission intensity lowered and reached a plateau which correlates to the emission intensity of plasmonic free system (SiO_2-[Ru]), suggesting that the influence of the plasmonic core becomes negligible.

Photocatalytic study

We then proceeded to the study of the photocatalytic activity of $Ag@SiO_2$-[Ru] NPs for the Schenck-ene reaction, specifically, the photooxidation of citronellol to the corresponding allylic hydroperoxydes (Scheme 1). The oxidation of citronellol was performed in a photoreactor illuminated with white LEDs using $Ag@SiO_2$-[Ru] with shell thicknesses ranging from 7 to 45 nm, under aerobic conditions in acetonitrile for 3 hours (Figure 3 blue and green).

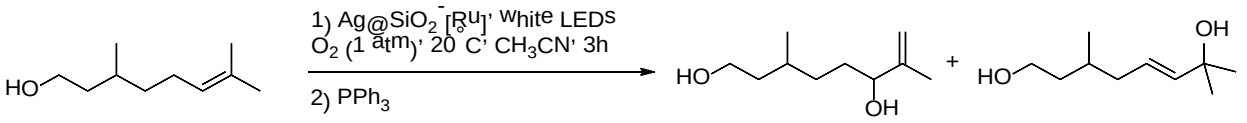

Scheme 1 - Reaction scheme for the oxidation of citronellol using $Ag@SiO_2$-[Ru] NPs. Standard reaction conditions: 0.33 mmol citronellol, CH_3CN, 3 h, O_2 balloon, 3.4 mmol% in $[Ru(bpy)_3]^{2+}$ for $Ag@SiO_2$-[Ru], white LED illumination.

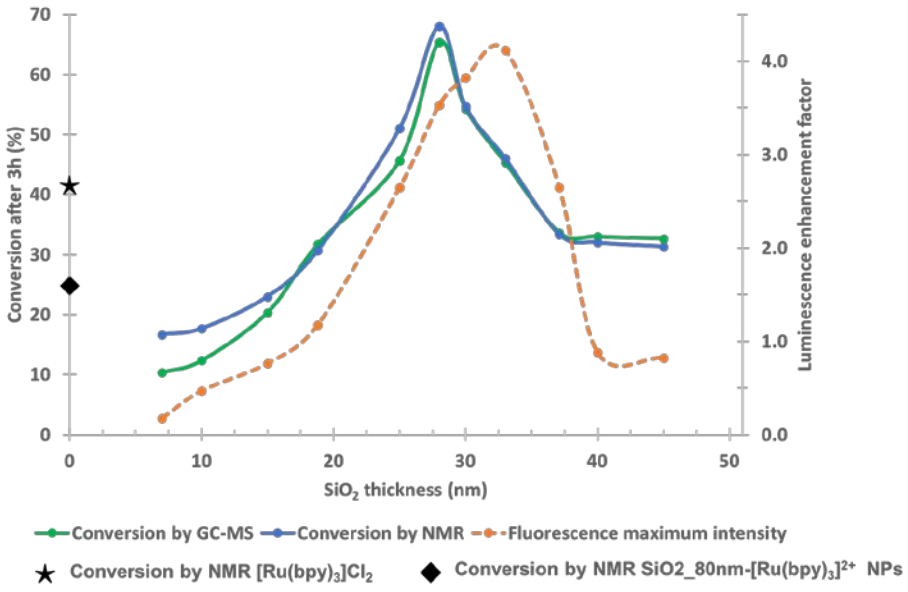

Figure 3 – Conversion of citronellol as determined by GC-MS (green) and NMR (blue) after 3h of reaction in comparison with the intensity of the luminescence measured for Ag@SiO_2-[Ru] NPs (orange), plotted as a function of SiO_2 shell thickness. Conversion by NMR for $[Ru(bpy)_3]Cl_2$ homogeneous (⋆) and $[Ru(bpy)_3]Cl_2$ immobilized on commercial SiO_2 NPs (◆). The molar catalytic loading was identical in all reactions (3.4 mmol%).

The formation of the desired alcohol regioisomers was monitored using GC-MS and ^{1}H NMR, following quenching of the peroxides by triphenylphosphine. The molar catalytic loading was selected to be 3.4 mmol% in $[Ru(bpy)_3]^{2+}$ in all cases discussed onwards, while maintaining the surface coverage equal for the Ag@SiO_2-[Ru] series. The effect of the plasmonic core on the photocatalyst is illustrated in Figure 4. Due to the SPR-induced field enhancement, the photocatalyst locally a higher electromagnetic field and the photoexcitation of $[Ru(bpy)_3]^{2+}$ increases. Relaxation (radiative or non-radiative) thus also increase. A proposed full reaction mechanism is provided in Figure S8. This mechanism is consistent with the fact the conversion was observed to grow linear as a function of light intensity (Figure S14).

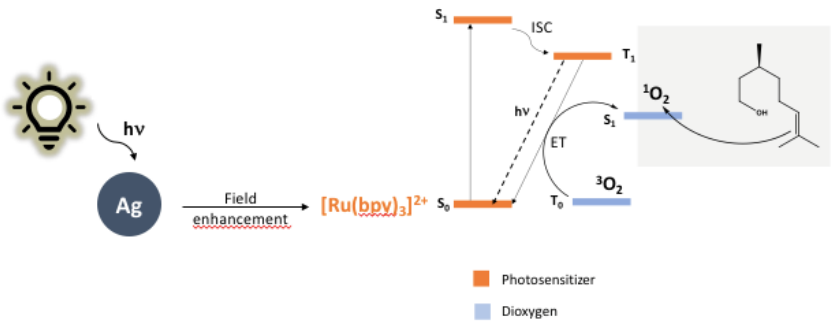

Figure 4 – Influence of the Ag NPs on the radiative and non-radiative rates of $[Ru(bpy)_3]^{2+}$ relaxation

In the following section, we used NMR yield values to compare the catalytic systems. When the reaction was carried out with homogeneous $[Ru(bpy)_3]Cl_2$ under the same molar catalytic loading as with the supported systems, it afforded a yield of 41%. When $[Ru(bpy)_3]Cl_2$ was immobilized on commercial SiO_2 NPs (SiO_2-[Ru] NPs), the yield dropped to 25% (Table S3). Such a drop is commonly observed for immobilized homogeneous catalysts.[80] We then turned to the reaction catalyzed by the Ag@SiO_2-[Ru] series. With thin SiO_2 shells, of 7 and 10 nm, conversions of 17 and 18 % were observed. They were lower than the conversion observed with SiO_2-[Ru] NPs, our model for non-plasmonic supported photocatalysts. As mentioned above, this result can be rationalized by the presence of the nearby Ag core which can quench the catalyst and negatively impact its activity. A similar drop in activity was observed when adding Ag NPs to a reaction solution containing homogenous $[Ru(bpy)_3]Cl_2$. In this case the conversion dropped from 41 % to 12 % (Table S3). We hypothesized that this could be due to either photo quenching or competitive absorption of light by the material, as observed by our group with an Fe(0) support.[73] As the shell thickness increased in the Ag@SiO_2-[Ru] series, conversion went up steadily, until a maximum conversion of 68 % was obtained for a SiO_2 thickness of 28 nm. This value is higher than the one observed with both homogeneous $[Ru(bpy)_3]Cl_2$ and SiO_2-[Ru] NPs. Specifically, this means that, at the maximum of plasmonic enhancement (Equation S5), the yield is improved by a factor of 2.6, as compared to the supporting on the simple SiO_2 NPs. Above a shell thickness of 28 nm the yields dropped rapidly and, beyond 35 nm, conversion plateaued at around 30 %, a value close to the performance of the simple SiO_2-[Ru] system. In this range, we reasoned that the effect of the SPR is very limited, thus explaining an activity comparable to photocatalysts immobilized on a non-plasmonic support. Control experiments show that almost no conversion occur under light irradiation in the absence of catalyst, or with Ag@SiO_2-[Ru] NPs without light irradiation (Table S3). When naked Ag NPs were used alone as catalyst, the conversion remained negligible. Previous study showed that Ag PNPs could directly catalyze the formation of $^1O_2$,[81-83] but in our hands, this did not prove to be efficient for the Schenck-ene process. GC-MS studies of the conversion over time suggest that the hybrid nanomaterial was stable during the length of the reaction (Figure S12).

Interestingly, the most intense luminescence of Ag@SiO_2-[Ru] was measured for a shell of 33 nm, while 28 nm of SiO_2 performed the best for the photocatalytic oxidation of citronellol. We have also checked the effect of the surface loading on catalysis at various shell thickness and confirmed that the most active system was at 0.53 µmol/g (Figure S13). A similar discrepancy in optimal shell thicknesses was observed by Heyne and coworkers when comparing the enhancement of the emission of a PNP enhanced photocatalyst (Rose Bengal) with its ability to produce $^1O_2$. While a 20 nm SiO_2 layer offered the highest luminescence for Ag@SiO_2-RB NPs, the maximum $^1O_2$ production was observed for a 11 nm silica shell.[48] We note that similarly to our system, the maximum for catalysis occurs for thinner shells than the maximum of the luminescence enhancement. Also, similar to this system, Heyne and coworkers reported that, at the peak of $^1O_2$ emission enhancement, the amount of $^1O_2$ available in solution is enhanced by a 3-fold factor. This values are in agreement with the 2.6 enhancement factor we observed. Other antenna-

photocatalyst systems employing a variety of metallic core, molecular dyes and spacing component have been developed. The characteristic of each system and the optimal spacing between the plasmon-active surface and the photocatalyst are detailed in section 5 of the ESI. A number of systems were developed with silica shells and they feature similar thicknesses for the maximum effect (most emission) in the range of 20-30 nm distances, similar to what we are reporting. A couple of systems do report much shorter distances, in the order of a few nm, one with silica[58] and one of a phospholipid layer.[56] At such short distances though, we did observe significant quenching, incompatible with high enhancement. The quenching of dye fluorescence close to PNPs has been extensively studied and confirms that with shell thicknesses of the order of 10 nm and lower significant quenching should take place.[84] This effect should be maximized when there is overlap between the LSPR and the dye excitation wavelength, which is the case here.[84] Beyond these values, plasmonic enhancement has been shown before to remain strong even into the long distances, all the way to 200 nm.[72] Our system is the sole one presenting such an optimization of the shell thickness in the context of catalysis (Table S4).[85]
Finally, it is well known that dyes coupled with PNPs excited at their LSPR wavelength do feature a reduction in their lifetime. This effect is associated as well with the broadening of the LSPR observed upon deposition of $[Ru(bpy)_3]^{2+}$ onto $Ag@SiO_2$.[84] We did not observe that this had any significant effect on catalytic results.

Based on the results on catalytic tests, we turned to electron energy loss spectroscopy (EELS) in order to better rationalise the optimal enhancement effect observed for a certain shell thickness.

Scanning transmission electron microscopy (STEM)- electron energy loss spectroscopy (EELS) study

Electron energy loss spectroscopy (EELS), used in conjunction with scanning transmission electron microscopy (STEM), is a powerful technique to map both bulk or surface plasmons intensity and energy. One of the advantages of STEM-EELS is to simultaneously provide both geospatial and energetic information of the surface plasmons.[86, 87] Using STEM-EELS, the surface plasmon energy of the naked Ag cores was measured to be 3.4 eV (365 nm), at the surface of the NPs (Figure S7).[88] This value is different from the SPR value obtained for the same systems by UV-Vis spectroscopy, because the STEM-EELS experiment takes place in ultra-high vacuum, and not in solution. This value is similar to results from previous studies on other Ag NPs, such as citrate-coated spheres, PVP-cubes, prisms, triangles, fractals, and wires.[89-92]

Coating Ag NPs with silica affected the surface plasmons, as it altered the dielectric medium around the PNP. Indeed, the energy of the surface plasmon measured at the surface of the NP decreased as a function of silica shell thickness(Figure S7).[88] For naked AgNPs, and $Ag@SiO_2$ with 7, 19 and 28 nm shells, we studied the intensity of the surface plasmon as a function of the distance to the Ag core (Figure 4). As expected, the intensity of the surface plasmon decreased exponentially in all cases. For no shell or a thin shell (7 nm), intensity was high and the decrease constant (Figure 4 grey and blue). For thicker shells (19 and 26 nm), there was a threshold effect, whereby almost no surface plasmon intensity was observed within the shell, while at the surface of the silica, intensity was restored and the signal decayed as a function of the distance like the

naked system (Figure 4 green and orange). Interestingly in the latter systems, the intensity at the SiO_2/vacuum interface was greater than at a similar distance from the plasmonic core for naked NPs and with a thin shell of 7 nm. Moreover, the LSPR peak shifted in energy as the silica shell became thicker, from 3.4 eV for naked Ag NPs down to 3.0 eV for a shell of 28 nm, which parallels the shift in the maximum of UV-Vis absorption shown in Figure 2. As STEM-EELS analysis are performed on individual particle, we selected NPs characteristic of the samples they belonged to. Analysis of shells larger than 30 nm could not be performed because the specimen was then too thick, preventing electrons from reaching the detector.[89]

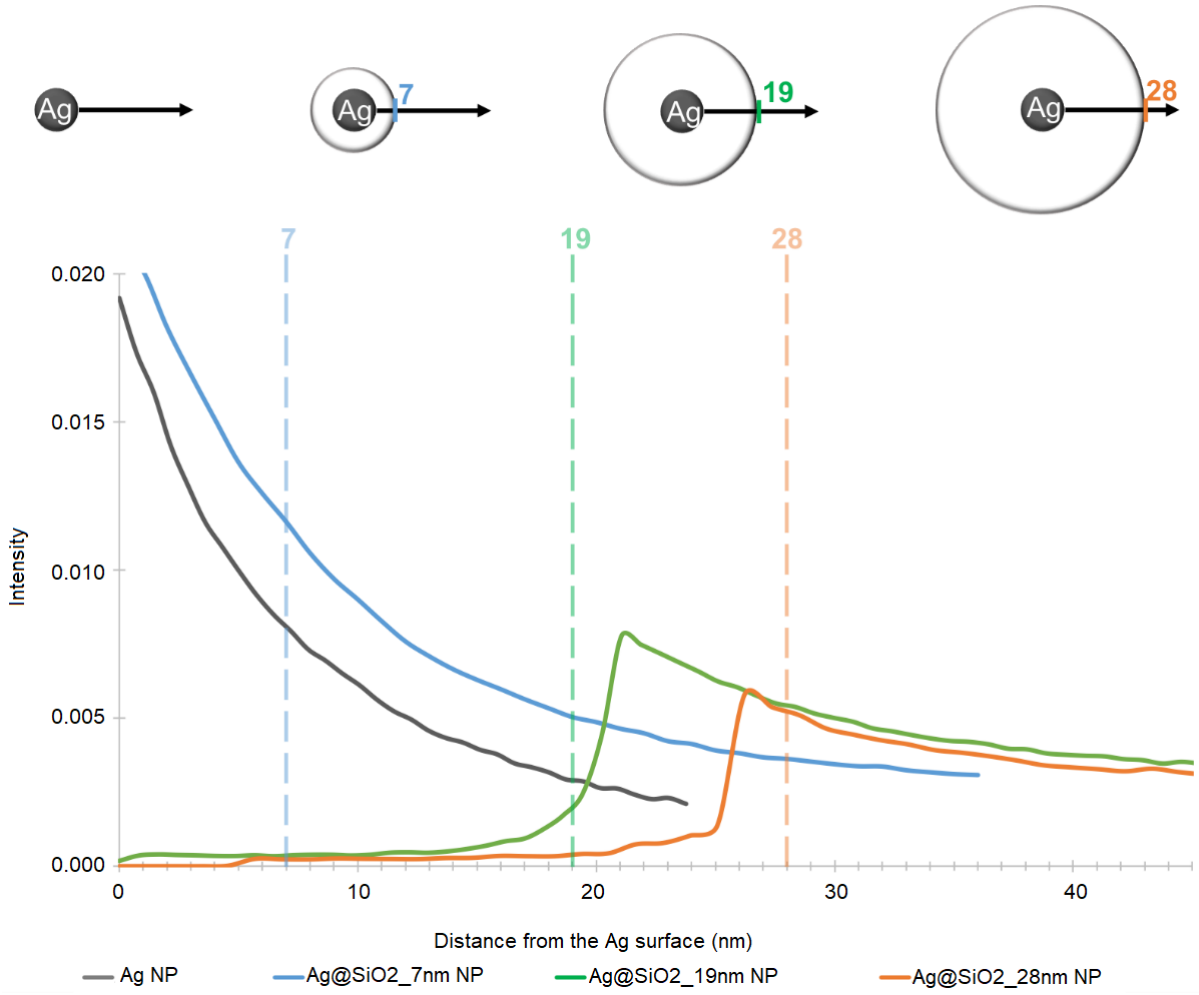

Figure 4 - Intensity of the LSPR peak measured by STEM-EELS at 3,4, 3.2, 3.0 and 3.0 eV, for naked Ag, Ag@SiO_2_7nm, Ag@SiO_2_19nm and Ag@SiO_2_28nm NP respectively, measured as a function of the distance from the Ag surface.

We then performed boundary element method (BEM) calculations with Matlab for metallic nanoparticles using MNPBEM toolbox[93, 94] on 80 nm Ag spheres with various thicknesses of SiO_2 shells, in order to simulate electron energy loss spectra and study the influence of the solvent on the surface plasmon energy position.

The energies determined by the simulations using a dielectric medium equals to 0 are similar to the ones obtained in the STEM experiment (I.e. under vacuum). Both simulation in vacuum and experimental data showed a peak centered at 3.4 eV for naked Ag NPs and a decreasing energy as a function of SiO_2 shell thickness (Figure 5A). By changing the value of the dielectric medium around the core shell NPs to mimic materials in a solvent, the general trend obtained is similar but the energies are altered by the environment surrounding the material. When switching from vacuum to CH_3CN, the trend is similar but there is a small shift in energy associated to the change in the dielectric environment (Figure 5B). In both media, when the thickness of the shell increases, the energy and the intensity decrease. Yet for thin silica layers, between 0 and 15 nm, a peak with a lower energy but more intense than for naked NPs is observed, similarly to data collected using STEM-EELS.

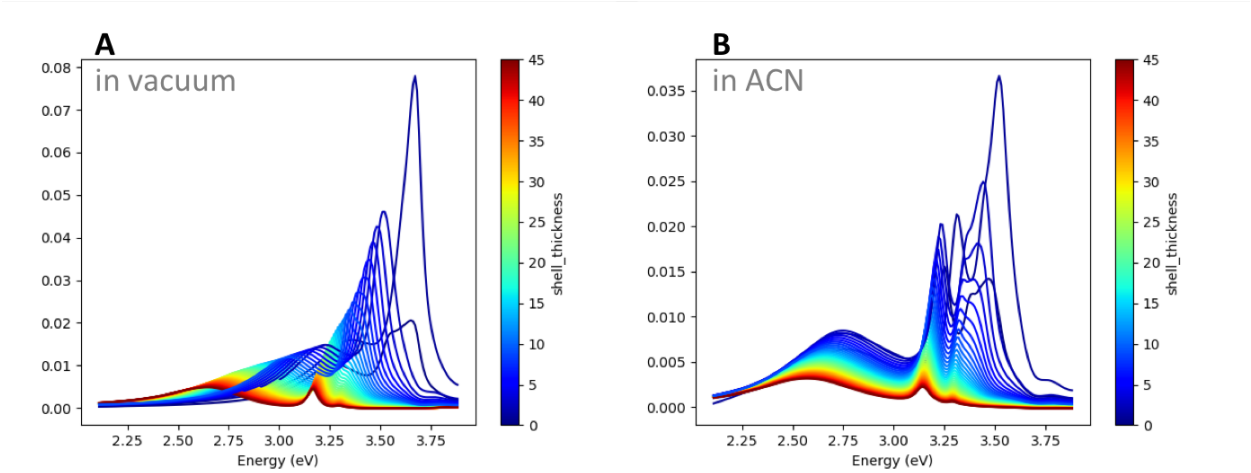

Figure 5 – Simulations of the intensity of the LSPR peaks at energies ranging between 2.25 and 3.75 eV for $Ag@SiO_2$ with shell ranging from 0 to 45 nm obtained with Matlab MNPBEM toolbox in vacuum (A) and in CH_3CN (B)

Despite some discrepancies in the energy values obtained by STEM-EELS, MNPBEM toolbox and UV-Vis spectroscopy, which can be attributed to the polydispersity of the NPs and the different dielectric media, similar trends in the energy decrease with increasing silica thickness were observed for the three methods. Even though, the intensity is dumped when going away from the metallic core, the plasmonic NP still has a significant impact in its surrounding environment as far as 40 nm away from its surface (Figure 6). Moreover, the intensity at the surface of the silica shell is particularly compelling for thicker coating. Thus higher conversions were observed for $Ag@SiO_2$-[Ru] NPs for which the separation between the photocatalyst and the plasmonic core was enough to avoid surface quenching but still offers an appealing enhanced electromagnetic field.

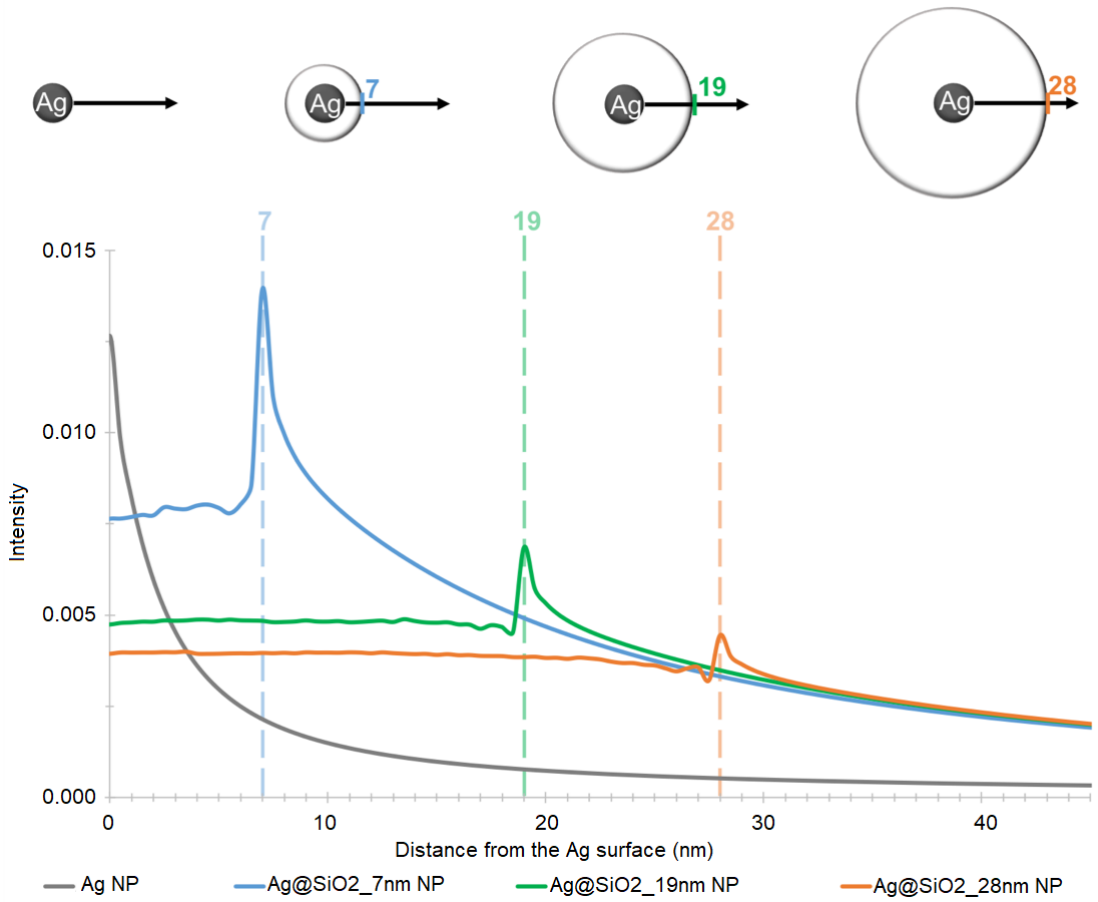

Figure 6 – Intensity of the LSPR peak calculated with Matlab MNPBEM toolbox in CH_3CN as a function of the distance from the Ag surface for naked Ag NPs and Ag@SiO_2 with 7, 19 and 28 nm shells

These results suggest that each component in the catalyst design is essential to efficient plasmonic enhancement. First, the Ag core allows the needed electro-magnetic field enhancement by SPR. Second, $[Ru(bpy)_3]^{2+}$ acted as the catalyst for the reaction. Third, both the core and fluorophores needed to be properly sheltered from one another by a thick enough silica shell, while the shell could not be too thick, otherwise the plasmon effect was too weak. Fourth, light was needed to activate both the SPR and the fluorophore itself. If any of these conditions was not met, catalysis was sub optimal. Like for the fluorescence study, we observed a maximum in catalysis activity for a medium shell thickness, namely at 28 nm. Thinner shells are less efficient, likely because of quenching. For larger ones, the SPR of the core is likely to be less effective.

Conclusion

In conclusion, we have synthesized a series of plasmonic nanoparticles coated with silica at various thicknesses and decorated with a photocatalyst (Ag@SiO_2-[Ru] NPs). This system allowed

for the first time a systematic study of the phosphorescence and the photocatalytic activity of these materials. The light-induced field enhancement in the vicinity of the plasmonic Ag NPs is responsible for the increased production of $^1O_2$ thus the catalytic activity of the $[Ru(bpy)_3]Cl_2$ towards the oxidation of alkenes. We have demonstrated an up to 4-fold activity increased compared to $[Ru(bpy)_3]Cl_2$ immobilized on SiO_2 NPs for nanomaterials with a 28 nm silica shell. Careful engineering of the hybrid plasmonic nanomaterial and the given photocatalyst is crucial as quenching of the photocatalyst was observed for thinner silica shells, while the photocatalyst was not affected by the LSPR for materials with thicker shells. Interestingly, EELS measurements and Matlab MNPBEM toolbox simulations revealed that even though there is an isolating layer, the intensity of the surface plasmons is strong at the interface between the silica layer and the photocatalyst, thus separation between the photocatalyst and the plasmonic core avoid surface quenching but still offers an appealing enhanced electromagnetic field in the photocatalyst's environment. The LSPR-induced field enhancement is the strongest at the surface of naked Ag NPs yet photocatalysts undergo quenching and for our $Ag@SiO_2$-[Ru] NPs, maximum luminescence emission and catalytic activity were observed for thicker silica coatings, for which the intensity of the surface plasmon is still significant.

Author contributions

AG, ZA and AM designed the project and experiments. AG and PG performed all the experiments. NB underwent the STEM-EELS experiments, which he interpreted with RG. FV designed and underwent the simulations. AG drafted the manuscript, with FV and NB and all authors edited it.

Acknowledgements

We thank the Natural Science and Engineering Research Council of Canada (NSERC) Discovery Grant and Discovery Accelerator Supplement, the Canada Foundation for Innovation (CFI), the Fonds France-Canada pour la Recherche (FFCR), the Fonds de Recherche du Québec – Nature et Technologies (FRQNT) Centre for Green Chemistry and Catalysis (CGCC) and McGill University for their financial support. We thank Dr. Boris Nijikovsky at the Facility for Electron Microscopy Research of McGill University for help in microscope operation and EDS data collection, the MC^2 facility at McGill University for help in acquiring NMR data, Galyna Shul from NanoUQAM for the zeta potential measurements and Dr. Ashlee Howarth for BET measurements. The authors thank Dr. Kevin Stamplecoskie for fruitful discussions.

Experimental section

All the chemicals were purchased from Sigma Aldrich and used as received.

Silver nanospheres were prepared using the protocol reported by Zhao *et al.*[95] with slight modifications. 18,0 mL of ethylene glycol (EG) was used to dissolved 0,90 g of polyvinylpyrrolidone (PVP) 30K MW 40K in a round bottom flask previously washed with aqua regia. 200 mg of $AgNO_3$ dissolved in 2,0 mL of EG were added to the PVP solution at room

temperature. After stirring at 145 °C for 4 h, 5 mL of acetone and 5 mL of ethanol were added, and the reaction mixture was let to cool down. The solution turned from colorless to green-brown when reaching the set temperature and the final solution was beige. The Ag NPs were washed three times using 30 mL of 50:50 acetone and ethanol mixture and centrifuged at 12 000 rpm at ambient conditions for 15 min. The resulting pellets were easily to suspend in ethanol and were dried in a vacuum oven at room temperature.

The Ag@SiO_2 NPs were obtained *via* base-catalyzed Stöber process. In a typical synthesis, 25 mg of Ag NPs were added to a round bottom flask containing 40 mL of ethanol, 10 mL of ultra-pure water and 1.25 mL of NH_4OH 30%. 25 µL of TEOS were added to the vigorously stirring solution at room temperature every 12 h until the SiO_2 layer reached the thickness wanted. Ag@SiO_2 NPs were isolated and purified by adding 20 mL of ethanol and centrifuged at 8 000 rpm for 10 min. The nanoparticles were washed two more times using 30 mL of ethanol and 10 mL of water prior to be suspended in ethanol and dried in a vacuum oven. The reaction was scaled up to 125 mg of Ag NPs by increasing the amount of reagents and solvents accordingly.

Immobilization of $[Ru(bpy)_3]Cl_2$ on Ag@SiO_2 NPs was realized following a procedure previously reported by the Amara group.[60] Briefly, an aqueous stock solution of $[Ru(bpy)_3]Cl_2.6H_2O$ 0.4 mM was prepared. A varied volume of this solution was then added to 20 mg of dried Ag@SiO_2 NPs suspended in a total volume of 3 mL of water. The volume added was calculated depending on the BET surface area in order to obtain the desired loading and surface coverage, which was identical of each nanomaterial. The solution was sonicated then stirred in the dark overnight. The final material was washed three times with water and dried by lyophilization. Complete immobilizations resulted in a colorless supernatant, which was confirmed by UV-Vis spectroscopy.

Photooxidation of citronellol was performed in a 125 mL 3-neck jacketed with a condenser, a thermometer and a balloon filed with oxygen were connected to the 3 necks, and the reactor was maintained at 20 °C using a water recirculatory (Figure S9). The reactor was illuminated by white LED strips (Ustellar UT33301) with a daylight white color (6000 K) positioned on a cylindrical support of about 30 cm diameter and 10 cm height and the whole set up was covered with aluminum foil.

In a typical procedure, 0.33 mmol of b-citronellol and 0.20 mmol of ortho-dimethoxybenzene (internal standard) were dissolved in 20 mL of acetonitrile, using part of the solvent to suspend 2.0 mg of Ag@SiO_2-Ru with a silica shell of 28 nm and surface loading equal to 6.5E-5 mmol of $[Ru(bpy)_3]^{2+}/m^2$. The amount of reagents was adapted to keep the concentration of molecular catalytic loading the same for all experiment while maintaining the concentration of PNPs identical, hence the opacity of the solution the same for all experiments.

For the kinetic studies, aliquots were taken every hour and quenched with 1.2 molar equivalent of triphenylphosphine and analyzed by GC-MS. After 3h, the reaction mixture was quenched with triphenylphosphine, concentrated by rotary evaporation and dissolved in $CDCl_3$ for ^1H NMR analysis.

Conversions were calculated using the ratio between the internal standard (ortho-dimethoxybenzene) and the reactant peak areas given by GC-MS at a given time, compared to the one at the beginning of the reaction. The conversion was also calculated using NMR by the ratio of the integration for the product and the internal standard. The reactions were performed in triplicate.

Supporting Information

List of the reagents and instruments used. Optimization of the synthesis of Ag NPs, Ag@SiO2 NPs, and Ag@SiO_2-[Ru] and their characterization: BET surface area and ζ-potential values, UV-Vis, emission and EELS spectra. Photocatalytic experimental conditions and data. Comparison with previous studies.

References

1. Ravelli, D.; Dondi, D.; Fagnoni, M.; Albini, A., Photocatalysis. A Multi-Faceted Concept for Green Chemistry. *Chem. Soc. Rev.* **2009,** *38* (7), 1999-2011.
2. Luo, J.; Zhang, S.; Sun, M.; Yang, L.; Luo, S.; Crittenden, J. C., A Critical Review on Energy Conversion and Environmental Remediation of Photocatalysts with Remodeling Crystal Lattice, Surface, and Interface. *ACS Nano* **2019,** *13* (9), 9811-9840.
3. McCullagh, C.; Skillen, N.; Adams, M.; Robertson, P. K., Photocatalytic Reactors for Environmental Remediation: A Review. *J. Chem. Technol. Biotechnol.* **2011,** *86* (8), 1002-1017.
4. König, B., Photocatalysis in Organic Synthesis–Past, Present, and Future. *Eur. J. Org. Chem.* **2017,** *2017* (15), 1979-1981.
5. Michelin, C.; Hoffmann, N., Photocatalysis Applied to Organic Synthesis–a Green Chemistry Approach. *Curr. Opin. Green Sustain. Chem.* **2018,** *10*, 40-45.
6. Ong, C. B.; Ng, L. Y.; Mohammad, A. W., A Review of Zno Nanoparticles as Solar Photocatalysts: Synthesis, Mechanisms and Applications. *Renew. Sust. Energy Rev.* **2018,** *81*, 536-551.
7. Wang, X.; Blechert, S.; Antonietti, M., Polymeric Graphitic Carbon Nitride for Heterogeneous Photocatalysis. *ACS Catal.* **2012,** *2* (8), 1596-1606.
8. Wang, J.-L.; Wang, C.; Lin, W., Metal–Organic Frameworks for Light Harvesting and Photocatalysis. *ACS Catal.* **2012,** *2* (12), 2630-2640.
9. Wang, J.-L.; Wang, C.; deKrafft, K. E.; Lin, W., Cross-Linked Polymers with Exceptionally High Ru (Bipy) 32+ Loadings for Efficient Heterogeneous Photocatalysis. *ACS Catal.* **2012,** *2* (3), 417-424.
10. Sharma, S.; Sharma, A., Recent Advances in Photocatalytic Manipulations of Rose Bengal in Organic Synthesis. *Org. Biomol. Chem.* **2019,** *17* (18), 4384-4405.

11. Twilton, J.; Zhang, P.; Shaw, M. H.; Evans, R. W.; MacMillan, D. W., The Merger of Transition Metal and Photocatalysis. *Nat. Rev. Chem.* **2017,** *1* (7), 1-19.
12. Yoon, T. P.; Ischay, M. A.; Du, J., Visible Light Photocatalysis as a Greener Approach to Photochemical Synthesis. *Nat. Chem.* **2010,** *2* (7), 527-532.
13. Teegardin, K.; Day, J. I.; Chan, J.; Weaver, J., Advances in Photocatalysis: A Microreview of Visible Light Mediated Ruthenium and Iridium Catalyzed Organic Transformations. *Org. Proc. Res. Dev.* **2016,** *20* (7), 1156-1163.
14. Kuramochi, Y.; Ishitani, O.; Ishida, H., Reaction Mechanisms of Catalytic Photochemical Co2 Reduction Using Re (I) and Ru (Ii) Complexes. *Coord. Chem. Rev.* **2018,** *373*, 333-356.
15. Luo, Q.; Mao, R.; Zhu, Y.; Wang, Y., Photoredox-Catalyzed Generation of Sulfamyl Radicals: Sulfonamidation of Enol Silyl Ether with Chlorosulfonamide. *J. Org. Chem.* **2019,** *84* (21), 13897-13907.
16. Sumino, S.; Uno, M.; Fukuyama, T.; Ryu, I.; Matsuura, M.; Yamamoto, A.; Kishikawa, Y., Photoredox-Catalyzed Hydrodifluoroalkylation of Alkenes Using Difluorohaloalkyl Compounds and a Hantzsch Ester. *J. Org. Chem.* **2017,** *82* (10), 5469-5474.
17. Chandrasekhar, D.; Borra, S.; Nanubolu, J. B.; Maurya, R. A., Visible Light Driven Photocascade Catalysis: Ru (Bpy) 3 (Pf6) 2/Tbhp-Mediated Synthesis of Fused B-Carbolines in Batch and Flow Microreactors. *Org. Lett.* **2016,** *18* (12), 2974-2977.
18. Juris, A.; Balzani, V.; Barigelletti, F.; Campagna, S.; Belser, P. l.; von Zelewsky, A. v., Ru (Ii) Polypyridine Complexes: Photophysics, Photochemistry, Eletrochemistry, and Chemiluminescence. *Coord. Chem. Rev.* **1988,** *84*, 85-277.
19. Cerfontaine, S.; Wehlin, S. A.; Elias, B.; Troian-Gautier, L., Photostable Polynuclear Ruthenium (Ii) Photosensitizers Competent for Dehalogenation Photoredox Catalysis at 590 Nm. *J. Am. Chem. Soc.* **2020,** *142* (12), 5549-5555.
20. Ghogare, A. A.; Greer, A., Using Singlet Oxygen to Synthesize Natural Products and Drugs. *Chem. Rev.* **2016,** *116* (17), 9994-10034.
21. Ravelli, D.; Protti, S.; Neri, P.; Fagnoni, M.; Albini, A., Photochemical Technologies Assessed: The Case of Rose Oxide. *Green Chem.* **2011,** *13* (7), 1876-1884.
22. Amara, Z.; Bellamy, J. F.; Horvath, R.; Miller, S. J.; Beeby, A.; Burgard, A.; Rossen, K.; Poliakoff, M.; George, M. W., Applying Green Chemistry to the Photochemical Route to Artemisinin. *Nat. Chem.* **2015,** *7* (6), 489-495.
23. Sheehan, F. Element Scarcity – Euchems Periodic Table. https://www.euchems.eu/euchems-periodic-table/ (accessed Feb. 5 2021).
24. Teixeira, R. I.; de Lucas, N. C.; Garden, S. J.; Lanterna, A. E.; Scaiano, J. C., Glass Wool Supported Ruthenium Complexes: Versatile, Recyclable Heterogeneous Photoredox Catalysts. *Catal. Sci. Technol.* **2020,** *10* (5), 1273-1280.
25. de Aberasturi, D. J.; Serrano-Montes, A. B.; Liz-Marzán, L. M., Modern Applications of Plasmonic Nanoparticles: From Energy to Health. *Adv. Opt. Mater.* **2015,** *3* (5), 602-617.
26. Li, J.-F.; Li, C.-Y.; Aroca, R. F., Plasmon-Enhanced Fluorescence Spectroscopy. *Chem. Soc. Rev.* **2017,** *46* (13), 3962-3979.
27. Mayer, K. M.; Hafner, J. H., Localized Surface Plasmon Resonance Sensors. *Chem. Rev.* **2011,** *111* (6), 3828-3857.
28. Ueno, K.; Oshikiri, T.; Sun, Q.; Shi, X.; Misawa, H., Solid-State Plasmonic Solar Cells. *Chem. Rev.* **2017,** *118* (6), 2955-2993.

29. Xiao, M.; Jiang, R.; Wang, F.; Fang, C.; Wang, J.; Jimmy, C. Y., Plasmon-Enhanced Chemical Reactions. *J. Mater. Chem. A* **2013,** *1* (19), 5790-5805.
30. Li, N.; Zhao, P.; Astruc, D., Anisotropic Gold Nanoparticles: Synthesis, Properties, Applications, and Toxicity. *Angew. Chem. Int. Ed.* **2014,** *53* (7), 1756-1789.
31. Lang, X.; Chen, X.; Zhao, J., Heterogeneous Visible Light Photocatalysis for Selective Organic Transformations. *Chem. Soc. Rev.* **2014,** *43* (1), 473-486.
32. Gellé, A.; Moores, A., Plasmonic Nanoparticles: Photocatalysts with a Bright Future. *Curr. Opin. Green Sustain. Chem.* **2018**, 60-66.
33. Gellé, A.; Jin, T.; de la Garza, L.; Price, G. D.; Besteiro, L. V.; Moores, A., Applications of Plasmon-Enhanced Nanocatalysis to Organic Transformations. *Chem. Rev.* **2019**, 986-1041.
34. Scaiano, J. C.; Stamplecoskie, K., Can Surface Plasmon Fields Provide a New Way to Photosensitize Organic Photoreactions? From Designer Nanoparticles to Custom Applications. *J. Phys. Chem. Let.* **2013,** *4* (7), 1177-1187.
35. Giannini, V.; Fernández-Domínguez, A. I.; Heck, S. C.; Maier, S. A., Plasmonic Nanoantennas: Fundamentals and Their Use in Controlling the Radiative Properties of Nanoemitters. *Chem. Rev.* **2011,** *111* (6), 3888-3912.
36. Wertz, E.; Isaacoff, B. P.; Flynn, J. D.; Biteen, J. S., Single-Molecule Super-Resolution Microscopy Reveals How Light Couples to a Plasmonic Nanoantenna on the Nanometer Scale. *Nano Lett.* **2015,** *15* (4), 2662-2670.
37. Darvill, D.; Centeno, A.; Xie, F., Plasmonic Fluorescence Enhancement by Metal Nanostructures: Shaping the Future of Bionanotechnology. *Phys. Chem. Chem. Phys* **2013,** *15* (38), 15709-15726.
38. Deng, W.; Goldys, E. M., Plasmonic Approach to Enhanced Fluorescence for Applications in Biotechnology and the Life Sciences. *Langmuir* **2012,** *28* (27), 10152-10163.
39. Deng, W.; Xie, F.; Baltar, H. T.; Goldys, E. M., Metal-Enhanced Fluorescence in the Life Sciences: Here, Now and Beyond. *Phys. Chem. Chem. Phys* **2013,** *15* (38), 15695-15708.
40. Willets, K. A.; Van Duyne, R. P., Localized Surface Plasmon Resonance Spectroscopy and Sensing. *Annu. Rev. Phys. Chem.* **2007,** *58*, 267-297.
41. Banholzer, M. J.; Millstone, J. E.; Qin, L.; Mirkin, C. A., Rationally Designed Nanostructures for Surface-Enhanced Raman Spectroscopy. *Chem. Soc. Rev.* **2008,** *37* (5), 885-897.
42. Zhang, C.; Zhao, H.; Zhou, L.; Schlather, A. E.; Dong, L.; McClain, M. J.; Swearer, D. F.; Nordlander, P.; Halas, N. J., Al–Pd Nanodisk Heterodimers as Antenna–Reactor Photocatalysts. *Nano Lett.* **2016,** *16* (10), 6677-6682.
43. Robatjazi, H.; Zhao, H.; Swearer, D. F.; Hogan, N. J.; Zhou, L.; Alabastri, A.; McClain, M. J.; Nordlander, P.; Halas, N. J., Plasmon-Induced Selective Carbon Dioxide Conversion on Earth-Abundant Aluminum-Cuprous Oxide Antenna-Reactor Nanoparticles. *Nat. Commun.* **2017,** *8* (1), 1-10.
44. Drexhage, K. H.; Kuhn, H.; Schäfer, F. P., Variation of the Fluorescence Decay Time of a Molecule in Front of a Mirror. *Ber. Bunsenges. Phys. Chem.* **1968,** *72* (2), 329-329.
45. Aslan, K.; Gryczynski, I.; Malicka, J.; Matveeva, E.; Lakowicz, J. R.; Geddes, C. D., Metal-Enhanced Fluorescence: An Emerging Tool in Biotechnology. *Curr. Opin. Biotechnol.* **2005,** *16* (1), 55-62.

46. Lakowicz, J. R.; Ray, K.; Chowdhury, M.; Szmacinski, H.; Fu, Y.; Zhang, J.; Nowaczyk, K., Plasmon-Controlled Fluorescence: A New Paradigm in Fluorescence Spectroscopy. *Analyst* **2008,** *133* (10), 1308-1346.
47. Zhang, J.; Fu, Y.; Chowdhury, M. H.; Lakowicz, J. R., Single-Molecule Studies on Fluorescently Labeled Silver Particles: Effects of Particle Size. *J. Phys. Chem. C* **2008,** *112* (1), 18-26.
48. Planas, O.; Macia, N.; Agut, M.; Nonell, S.; Heyne, B., Distance-Dependent Plasmon-Enhanced Singlet Oxygen Production and Emission for Bacterial Inactivation. *J. Am. Chem. Soc.* **2016,** *138* (8), 2762-2768.
49. Macia, N.; Kabanov, V.; Heyne, B., Rationalizing the Plasmonic Contributions to the Enhancement of Singlet Oxygen Production. *J. Phys. Chem. C* **2020,** *124* (6), 3768-3777.
50. Macia, N.; Bresoli-Obach, R.; Nonell, S.; Heyne, B., Hybrid Silver Nanocubes for Improved Plasmon-Enhanced Singlet Oxygen Production and Inactivation of Bacteria. *J. Am. Chem. Soc.* **2018,** *141* (1), 684-692.
51. Mendoza, C.; Désert, A.; Chateau, D.; Monnereau, C.; Khrouz, L.; Lerouge, F.; Andraud, C.; Monbaliu, J.-C. M.; Parola, S.; Heinrichs, B., Au Nanobipyramids@Msio2 Core–Shell Nanoparticles for Plasmon-Enhanced Singlet Oxygen Photooxygenations in Segmented Flow Microreactors. *Nanoscale Adv.* **2020,** *2* (11), 5280-5287.
52. Yin, N.; Liu, Y.; Liu, L.; Lei, J.; Jiang, T.; Wang, H.; Zhu, L.; Xu, X., Fluorescence Enhancement of Ru(Bpy)32+ by Core–Shell Ag@Sio2 Nanocomposites. *J. Alloys Compd.* **2013,** *581*, 6-10.
53. Tovmachenko, O. G.; Graf, C.; van den Heuvel, D. J.; van Blaaderen, A.; Gerritsen, H. C., Fluorescence Enhancement by Metal-Core/Silica-Shell Nanoparticles. *Adv. Mater.* **2006,** *18* (1), 91-95.
54. Cheng, D.; Xu, Q.-H., Separation Distance Dependent Fluorescence Enhancement of Fluorescein Isothiocyanate by Silver Nanoparticles. *Chem. Commun.* **2007,** (3), 248-250.
55. Bardhan, R.; Grady, N. K.; Cole, J. R.; Joshi, A.; Halas, N. J., Fluorescence Enhancement by Au Nanostructures: Nanoshells and Nanorods. *ACS Nano* **2009,** *3* (3), 744-752.
56. An, X.; Stelter, D.; Keyes, T.; Reinhard, B. M., Plasmonic Photocatalysis of Urea Oxidation and Visible-Light Fuel Cells. *Chem* **2019,** *5* (8), 2228-2242.
57. Chen, Y.; Munechika, K.; Ginger, D. S., Dependence of Fluorescence Intensity on the Spectral Overlap between Fluorophores and Plasmon Resonant Single Silver Nanoparticles. *Nano Lett.* **2007,** *7* (3), 690-696.
58. Mori, K.; Kawashima, M.; Che, M.; Yamashita, H., Enhancement of the Photoinduced Oxidation Activity of a Ruthenium(Ii) Complex Anchored on Silica-Coated Silver Nanoparticles by Localized Surface Plasmon Resonance. *Angew. Chem.* **2010,** *122* (46), 8780-8783.
59. Linic, S.; Chavez, S.; Elias, R., Flow and Extraction of Energy and Charge Carriers in Hybrid Plasmonic Nanostructures. *Nat. Mater.* **2021**, 1-9.
60. Tambosco, B.; Segura, K.; Seyrig, C.; Cabrera, D.; Port, M.; Ferroud, C.; Amara, Z., Outer-Sphere Effects in Visible-Light Photochemical Oxidations with Immobilized and Recyclable Ruthenium Bipyridyl Salts. *ACS Catal.* **2018,** *8* (5), 4383-4389.
61. Blanchard, V.; Asbai, Z.; Cottet, K.; Boissonnat, G.; Port, M.; Amara, Z., Continuous Flow Photo-Oxidations Using Supported Photocatalysts on Silica. *Org. Proc. Res. Dev.* **2020,** *24* (5), 822-826.

62. Macia, N.; Kabanov, V.; Côté-Cyr, M.; Heyne, B., Roles of near and Far Fields in Plasmon-Enhanced Singlet Oxygen Production. *J. Phys. Chem. Let.* **2019,** *10* (13), 3654-3660.
63. Szmacinski, H.; Lakowicz, J. R.; Catchmark, J. M.; Eid, K.; Anderson, J. P.; Middendorf, L., Correlation between Scattering Properties of Silver Particle Arrays and Fluorescence Enhancement. *Appl. Spectrosc.* **2008,** *62* (7), 733-738.
64. Wu, C.; Mosher, B. P.; Lyons, K.; Zeng, T., Reducing Ability and Mechanism for Polyvinylpyrrolidone (Pvp) in Silver Nanoparticles Synthesis. *J. Nanosci. Nanotechnol.* **2010,** *10* (4), 2342-2347.
65. Kobayashi, Y.; Katakami, H.; Mine, E.; Nagao, D.; Konno, M.; Liz-Marzán, L. M., Silica Coating of Silver Nanoparticles Using a Modified Stöber Method. *J. Colloid Interface Sci.* **2005,** *283* (2), 392-396.
66. Matsui, K.; Momose, F., Luminescence Properties of Tris (2, 2 '-Bipyridine) Ruthenium (Ii) in Sol− Gel Systems of Sio2. *Chem. Mater.* **1997,** *9* (11), 2588-2591.
67. Innocenzi, P.; Kozuka, H.; Yoko, T., Fluorescence Properties of the Ru (Bpy) 32+ Complex Incorporated in Sol− Gel-Derived Silica Coating Films. *J. Phys. Chem. B* **1997,** *101* (13), 2285-2291.
68. Liz-Marzán, L. M., Tailoring Surface Plasmons through the Morphology and Assembly of Metal Nanoparticles. *Langmuir* **2006,** *22* (1), 32-41.
69. Wertz, E. A.; Isaacoff, B. P.; Biteen, J. S., Wavelength-Dependent Super-Resolution Images of Dye Molecules Coupled to Plasmonic Nanotriangles. *ACS Photonics* **2016,** *3* (10), 1733-1740.
70. Abadeer, N. S.; Brennan, M. R.; Wilson, W. L.; Murphy, C. J., Distance and Plasmon Wavelength Dependent Fluorescence of Molecules Bound to Silica-Coated Gold Nanorods. *ACS Nano* **2014,** *8* (8), 8392-8406.
71. Hu, B.; Cao, X.; Nahan, K.; Caruso, J.; Tang, H.; Zhang, P., Surface Plasmon-Photosensitizer Resonance Coupling: An Enhanced Singlet Oxygen Production Platform for Broad-Spectrum Photodynamic Inactivation of Bacteria. *J. Mater. Chem. B* **2014,** *2* (40), 7073-7081.
72. Kedem, O.; Wohlleben, W.; Rubinstein, I., Distance-Dependent Fluorescence of Tris (Bipyridine) Ruthenium (Ii) on Supported Plasmonic Gold Nanoparticle Ensembles. *Nanoscale* **2014,** *6* (24), 15134-15143.
73. Terra, J. C.; Desgranges, A.; Monnereau, C.; Sanchez, E. H.; De Toro, J. A.; Amara, Z.; Moores, A., Photocatalysis Meets Magnetism: Designing Magnetically Recoverable Supports for Visible-Light Photocatalysis. *ACS Appl. Mater. Inter.* **2020,** *12* (22), 24895-24904.
74. Banholzer, M. J.; Harris, N.; Millstone, J. E.; Schatz, G. C.; Mirkin, C. A., Abnormally Large Plasmonic Shifts in Silica-Protected Gold Triangular Nanoprisms. *J. Phys. Chem. C* **2010,** *114* (16), 7521-7526.
75. Rodríguez-Fernández, J.; Pastoriza-Santos, I.; Perez-Juste, J.; García de Abajo, F. J.; Liz-Marzan, L. M., The Effect of Silica Coating on the Optical Response of Sub-Micrometer Gold Spheres. *J. Phys. Chem. C* **2007,** *111* (36), 13361-13366.
76. Pastoriza-Santos, I.; Gomez, D.; Pérez-Juste, J.; Liz-Marzán, L. M.; Mulvaney, P., Optical Properties of Metal Nanoparticle Coated Silica Spheres: A Simple Effective Medium Approach. *Phys. Chem. Chem. Phys* **2004,** *6* (21), 5056-5060.

77. Aslam, U.; Chavez, S.; Linic, S., Controlling Energy Flow in Multimetallic Nanostructures for Plasmonic Catalysis. *Nat. Nanotechnol.* **2017,** *12* (10), 1000-1005.
78. Chavez, S.; Aslam, U.; Linic, S., Design Principles for Directing Energy and Energetic Charge Flow in Multicomponent Plasmonic Nanostructures. *ACS Energy Lett.* **2018,** *3* (7), 1590-1596.
79. Chavez, S.; Rao, V. G.; Linic, S., Unearthing the Factors Governing Site Specific Rates of Electronic Excitations in Multicomponent Plasmonic Systems and Catalysts. *Faraday Discuss.* **2019,** *214*, 441-453.
80. Cole-Hamilton, D. J.; Tooze, R. P., *Catalyst Separation, Recovery and Recycling: Chemistry and Process Design*. Springer Science & Business Media: 2006; Vol. 30.
81. Vankayala, R.; Sagadevan, A.; Vijayaraghavan, P.; Kuo, C.-L.; Hwang, K. C., Metal Nanoparticles Sensitize the Formation of Singlet Oxygen. *Angew. Chem. Int. Ed.* **2011,** *50* (45), 10640-10644.
82. Toftegaard, R.; Arnbjerg, J.; Daasbjerg, K.; Ogilby, P. R.; Dmitriev, A.; Sutherland, D. S.; Poulsen, L., Metal-Enhanced 1270 Nm Singlet Oxygen Phosphorescence. *Angew. Chem. Int. Ed.* **2008,** *47* (32), 6025-6027.
83. Huang, Y. F.; Zhang, M.; Zhao, L. B.; Feng, J. M.; Wu, D. Y.; Ren, B.; Tian, Z. Q., Activation of Oxygen on Gold and Silver Nanoparticles Assisted by Surface Plasmon Resonances. *Angew. Chem. Int. Ed.* **2014,** *53* (9), 2353-2357.
84. Reineck, P.; Gómez, D.; Ng, S. H.; Karg, M.; Bell, T.; Mulvaney, P.; Bach, U., Distance and Wavelength Dependent Quenching of Molecular Fluorescence by Au@ Sio2 Core–Shell Nanoparticles. *ACS Nano* **2013,** *7* (8), 6636-6648.
85. Maier, S. A., *Plasmonics: Fundamentals and Applications*. Springer Science & Business Media: 2007.
86. Wu, Y.; Li, G.; Camden, J. P., Probing Nanoparticle Plasmons with Electron Energy Loss Spectroscopy. *Chem. Rev.* **2017,** *118* (6), 2994-3031.
87. Kociak, M.; Stéphan, O., Mapping Plasmons at the Nanometer Scale in an Electron Microscope. *Chem. Soc. Rev.* **2014,** *43* (11), 3865-3883.
88. Moores, A.; Goettmann, F., The Plasmon Band in Noble Metal Nanoparticles: An Introduction to Theory and Applications. *New J. Chem.* **2006,** *30* (8), 1121-1132.
89. Brodusch, N.; Demers, H.; Gellé, A.; Moores, A.; Gauvin, R., Electron Energy-Loss Spectroscopy (Eels) with a Cold-Field Emission Scanning Electron Microscope at Low Accelerating Voltage in Transmission Mode. *Ultramicroscopy* **2019,** *203*, 21-36.
90. Bicket, I. C.; Bellido, E. P.; McRae, D. M.; Lagugné-Labarthet, F.; Botton, G. A., Carving Plasmon Modes in Silver Sierpinski Fractals. *ACS Photonics* **2019,** *6* (11), 2974-2984.
91. Wang, W.; Yang, Q.; Fan, F.; Xu, H.; Wang, Z. L., Light Propagation in Curved Silver Nanowire Plasmonic Waveguides. *Nano Lett.* **2011,** *11* (4), 1603-1608.
92. Koh, A. L.; Bao, K.; Khan, I.; Smith, W. E.; Kothleitner, G.; Nordlander, P.; Maier, S. A.; McComb, D. W., Electron Energy-Loss Spectroscopy (Eels) of Surface Plasmons in Single Silver Nanoparticles and Dimers: Influence of Beam Damage and Mapping of Dark Modes. *ACS Nano* **2009,** *3* (10), 3015-3022.
93. Hohenester, U., Simulating Electron Energy Loss Spectroscopy with the Mnpbem Toolbox. *Comput. Phys. Commun.* **2014,** *185* (3), 1177-1187.

94. De Abajo, F. G.; Howie, A., Retarded Field Calculation of Electron Energy Loss in Inhomogeneous Dielectrics. *Phys. Rev. B* **2002,** *65* (11), 115418-115435.
95. Zhao, T.; Sun, R.; Yu, S.; Zhang, Z.; Zhou, L.; Huang, H.; Du, R., Size-Controlled Preparation of Silver Nanoparticles by a Modified Polyol Method. *Colloids Surf. A Physicochem. Eng.* **2010,** *366* (1-3), 197-202.

TOC